Modulational instability in $\mathcal{PT}$-symmetric Bragg grating structures with saturable nonlinearity

K. Tamilselvan,[1,*] A. Govindarajan,[1,*,†] I. Inbavalli,[2] T. Alagesan,[2] and M. Lakshmanan[1]
[1]*Department of Nonlinear Dynamics, School of Physics, Bharathidasan University, Tiruchirappalli 620 024, India*
[2]*Department of Physics, Presidency College (Autonomous), Chennai 600 005, India*

(Received 18 January 2023; accepted 4 April 2023; published 12 May 2023)

We investigate the nontrivial characteristics of modulational instability (MI) in a system of Bragg gratings with saturable nonlinearity. We also introduce an equal amount of gain and loss into the existing system, which gives rise to an additional degree of freedom, due to the concept of $\mathcal{PT}$ symmetry. We obtain the nonlinear dispersion relation of the saturable model and discover that such dispersion relations for both the conventional and $\mathcal{PT}$-symmetric cases contradict the conventional Kerr and saturable systems by not displaying the typical signature of loop formation in either the upper branch or lower branch of the curve drawn against the wave number and detuning parameter. We employ a standard linear stability analysis to study the MI dynamics of the continuous waves perturbed by an infinitesimal perturbation. The main objective of this paper is twofold: We investigate the dynamics of the MI gain spectrum at the top and bottom of the photonic band gap followed by a comprehensive analysis carried out in the anomalous and normal dispersion regimes. As a result, this perturbed system driven by the saturable nonlinearity and gain or loss yields a variety of instability spectra, which include the conventional sidebands, monotonically increasing gain, the emergence of a single spectrum in either of the Stokes wave-number regions, and so on. In particular, we observe a remarkably peculiar spectrum, which is caused predominantly by the system parameter, though the perturbation wave number boosts the former. We also address the impact of all the physical parameters considered in the proposed model, which include the coupling coefficient, dispersion parameter, and saturable nonlinearity on the phenomenon of MI for different $\mathcal{PT}$-symmetric regimes ranging from the unbroken one to the broken one in greater detail.

DOI: 10.1103/PhysRevA.107.053510

I. INTRODUCTION

Bender and Boettcher introduced the concept of parity ($\mathcal{P}$) and time ($\mathcal{T}$) symmetry to prove the conjecture which was put forward by Bessis in field theory (see [1–3] and references therein), which then stimulated unprecedented interest across a wide range of fields in physics, including optics [4–9], photonics [10,11], and condensed-matter physics [12]. In quantum mechanics, the concept was introduced to demonstrate that a non-Hermitian Hamiltonian can admit eigenvalues of real energy spectra when the operators $\mathcal{P}$ and $\mathcal{T}$ are applied simultaneously. It was later demonstrated that the realization of the $\mathcal{PT}$ symmetry can be achieved in optics by the practical inclusion of a complex refractive index with equal gain or loss profile in optical systems [4]. As is well known, the distribution of a complex refractive index in an optical system is defined by $n(x) = n_R(x) + in_I(x)$, meaning that the index profile will be $\mathcal{PT}$ symmetric if the real and imaginary components of the index profile are equal to an even function $n_R(x) = n_R(-x)$ and an odd function $n_I(x) = -n_I(-x)$, respectively [4,5,7]. This concept has been experimentally observed in several physical settings, including coupled waveguides and synthetic photonic lattices [7,10]. In non-Hermitian $\mathcal{PT}$ symmetry, there exists a distinct phase-transition point at which the eigenvalue shifts from real to imaginary in its energy levels. [7]. In the presence of a certain $\mathcal{PT}$-symmetric threshold level, in particular, below the phase-transition point, the system becomes stable, referred to as the unbroken-$\mathcal{PT}$-symmetric regime, and above the $\mathcal{PT}$-threshold level, the system exhibits an exponential growth in its energy, thereby leading the former to an unstable state and eventually leading to spontaneous symmetry breaking. This unstable region is then known as the broken-$\mathcal{PT}$-symmetric regime [13]. The phase transition of $\mathcal{PT}$ symmetry is the key phenomenon underpinning the existence of different kinds of unusual dynamics, including nonreciprocity [6] and double refraction [5]. These advances in $\mathcal{PT}$ symmetry would enable the design of novel artificial optical systems that include periodic optical systems involving optical gain and loss profile periodic lattices, coupled structures, and passive experimental arrangements [14–16].

The propagation of light in periodic structures, particularly in fiber Bragg gratings (FBGs), offers a number of highly versatile platforms for achieving a wide range of lightwave telecommunication applications. These include wavelength-stabilized pump lasers, dispersion compensators, narrowband filters, and add-drop multiplexers [17,18], to name a few. In the conventional FBG, the refractive index of the fiber is systematically altered by an intracore Bragg grating, while the FBG operates in the ultraviolet region [18,19]. To date, two distinct theories have been proposed to explain the propagation of light in FBGs: standard coupled-mode theory, which

*These authors contributed equally to this work.
†Corresponding author: govin.nld@gmail.com

explains the propagation of forward and backward waves in a variety of distributed feedback structures [20], and the less-known Bloch-wave theory, which describes electron motion in semiconductors [21]. The photonic band gap, as in the linear domain, refers to the amount of chromatic dispersion present in the FBG, also known as the stop band since the light transmission over a range of frequency is restricted by the band-gap region [21–23]. There are many exciting phenomena that result from the combination of linear dispersion resulting from the band gap and nonlinearity introduced by the waveguide material, including Bragg solitons [24], gap solitons [25,26], optical switching [27], pulse compression [28], optical bi- and multistability [29], and modulational instability [30]. Recently, the notion of $\mathcal{PT}$ symmetry was realized in FBGs in order to demonstrate the dynamic behavior of localized structures [31]. The formation and stable dynamics of solitons in $\mathcal{PT}$-symmetric FBGs for different kinds of linear effects and corresponding spectra have been extensively studied [15]. Also, exactly solvable Dirac Hamiltonians are constructed by employing the confluent Crum-Darboux transformation in the $\mathcal{PT}$-symmetric Bragg gratings [32]. Moreover, the concept of $\mathcal{PT}$ symmetry provides a stable platform for the development of various intriguing features, including unidirectional wave transport at exceptional points [33], coherent complete absorption in coupled resonators [34], and nonreciprocal dynamics [6]. The role of $\mathcal{PT}$ symmetry has also been realized in linear FBG settings as a result of periodic modulation of the index and gain profiles which lead to a number of exotic dynamics such as asymmetrical mode coupling manifesting in unique reflection and transmission spectra. In particular, there is a single reflection peak if the light is launched from the left end, while it becomes transparent on the rear end, which means that it does not reflect at all [35,36].

Modulation instability (MI) is a phenomenon that precedes the formation of localized modes in almost all nonlinear media, including FBGs. It is well known that MI leads to an exponential growth of the continuous wave (cw) as a consequence of a small perturbation imposed on it and eventually it breaks up into a train of localized ultrashort pulses [37,39]. This phenomenon originated in fluid dynamics as Benjamin-Feir instability [40] and then spread to a variety of other fields, including optics [37,38], solid-state physics [41], plasma physics [42], and electrical lines [41]. As a result of MI dynamics, prominent light-matter interactions are stimulated, which include phenomena such as Fermi-Pasta-Ulam-Tsingou recurrence in optics [43] and the formation of Akhmediev breathers and Peregrine solitons [44], which can further be witnessed through the nonlinear stage of MI in optical fibers [45,46]. The implementation of MI could be utilized to achieve several potential applications, including the generation of ultrashort pulse trains at terahertz frequencies with high repetition rates [47], the generation of supercontinuum [48], and the development of optical frequency combs [49,50]. These intriguing characteristics of the MI phenomenon in fiber optics have been investigated both theoretically and analytically in a wide range of nonlinear media and have also been extended to emerging areas such as negative index materials and $\mathcal{PT}$-symmetric media [51].

It is important to note that the studies on MI have been quite extensively investigated in conventional FBGs, such as Kerr and non-Kerr nonlinear media, and apodized grating structures in which the cw states are then converted into a train of ultrashort pulses [30,52,53]. As with other nonlinear media, saturable nonlinear media play a prominent role not only in the formation of stable solitons but also in the MI dynamics, where the nonlinear saturable parameter has a substantial impact on the MI gain spectrum and its bandwidth. By and large, the refractive index of a saturable nonlinear medium increases with the intensity I, whereas it becomes saturated when the system is exposed to a sufficiently high level of input intensity [54,55]. In a Kerr-like medium, this saturable nonlinearity is typically characterized by its nonlinear refractive index $[n_{\rm nl}(I)]$ profile, such as $n_{\rm nl}(I) = n_\infty[1 - 1/(1 + I/I_{\rm sat})]$ (where $I_{\rm sat}$ and n_∞ indicate the saturation intensity and the maximum change in the refractive index, respectively). A considerable amount of attention has been paid to this type of nonlinearity [56,57]. In particular, the saturable nonlinearity plays a very important role in preventing the catastrophic collapse of the nonlinear Schrödinger equation in higher dimensions [57]. Also, such a saturable nonlinear medium supports the existence of stable localized solitons in various physical settings, such as two-level atomic systems [54] and photorefractive materials like photovoltaic $LiNbO_3$ [58]. Along these lines, the impact of saturable nonlinearity has been thoroughly analyzed in the ubiquitous process of MI in the framework of nonlinear optics, in particular, semiconductor-doped glass fibers and optical fibers [55,59,60]. In the context of FBGs, the saturable nonlinearity has also been used to study the existence and stability of various types of solitons. The physical mechanism to realize such a model in the spatial region has also been put forward by using a planar waveguide composed of photorefractive material with a longitudinal diffraction lattice written in its cladding [61]. Although there exists a great deal of research on the conventional FBGs, barring a single work [62], there seems to be no work dealing with the study of MI in the $\mathcal{PT}$-symmetric FBG in the literature. In addition, there is no study emphasizing the impact of saturable nonlinearity on the MI dynamics in both conventional and $\mathcal{PT}$-symmetric media. With these considerations in mind, in this paper we carry out an extensive study elucidating the importance of saturable parameters in both conventional and $\mathcal{PT}$-symmetric settings.

Following the detailed explanation of the proposed model in Sec. II, the analytical procedure of the linear stability analysis which is employed for the investigation of MI is provided in Sec. III. In Sec. IV we then examine the dynamics of the MI gain spectrum near the edges of the photonic band-gap and normal and anomalous dispersion regimes. Each of these cases is analyzed for the effect of various physical parameters, including gain or loss and saturable nonlinearity under different $\mathcal{PT}$-symmetric regimes. We conclude our findings with a detailed summary in Sec. V.

II. MODEL

We consider $\mathcal{PT}$-symmetric fiber Bragg gratings with a period Λ imprinted on the core of the fiber of refractive index n_0 and length z. Mathematically, the distribution of the refractive index $[n(z)]$ profile for a $\mathcal{PT}$ FBG with saturable nonlinear

media can be described as follows [63]:

$$n(z) = n_0 + n_{1R}\cos\left(\frac{2\pi z}{\Lambda}\right) + in_{1I}\sin\left(\frac{2\pi z}{\Lambda}\right) - n_2 \mathscr{f}(|E|^2). \tag{1}$$

Here n_1 represents the strength of the modulation parameter and its real and imaginary parts are indicated through terms n_{1R} and n_{1I}, respectively, which are responsible for the $\mathcal{PT}$-symmetric potential. The term n_2 represents the nonlinear refractive index pertaining to the saturable nonlinearity of the Bragg structure. The function $\mathscr{f}(|E|^2)$ can be expressed as $1/(1+|E|^2)$, where E stands for the optical field [61]. By taking the square of the above nonlinear refractive index profile (1) and neglecting the higher-order terms in n_1 and n_2, one can obtain the reduced form

$$n^2(z) = n_0^2 + 2n_0 n_{1R}\cos\left(\frac{2\pi z}{\Lambda}\right) + 2in_{1R}n_{1I}\sin\left(\frac{2\pi z}{\Lambda}\right) - 2n_0 n_2 \mathscr{f}(|E|^2). \tag{2}$$

The dynamics of the system under study can be modeled by the time-dependent Helmholtz equation for the optical field E as

$$\frac{\partial^2 E}{\partial z^2} + \frac{\partial^2 E}{\partial t^2} + k^2\frac{n^2(z)}{n_0^2}E = 0, \tag{3}$$

where k represents the wave vector. We seek an optical field $E(z,t)$ that consists of forward and backward components propagating inside the FBG as

$$E(z,t) = \Psi_1(z,t)\exp[i(kz-\omega_0 t)] + \Psi_2(z,t)\exp[-i(kz-\omega_0 t)], \tag{4}$$

where the terms $\Psi_1(z,t)$ and $\Psi_2(z,t)$ indicate slowly varying amplitudes of the forward and backward electric fields, respectively and ω_0 indicates the frequency of the incident light. Substituting Eq. (4) into Eq. (3) and applying the synchronous approximation, one can obtain the normalized coupled-mode equations with the saturable nonlinearity and equal amounts of gain and loss as [26,61]

$$i\left(\frac{\partial\Psi_1}{\partial z} + \frac{1}{v}\frac{\partial\Psi_1}{\partial t}\right) + (\kappa+g)\Psi_2 - \mathscr{f}(|\Psi_{1,2}|)\Psi_1 = 0, \tag{5a}$$

$$-i\left(\frac{\partial\Psi_2}{\partial z} - \frac{1}{v}\frac{\partial\Psi_2}{\partial t}\right) + (\kappa-g)\Psi_1 - \mathscr{f}(|\Psi_{1,2}|)\Psi_2 = 0, \tag{5b}$$

where the group velocity of light is given by $v_g = c/n$. Here c indicates the speed of light and the nonlinear term $\mathscr{f}(|\Psi_{1,2}|^2)$ can be expressed as $\Gamma/(1+|\Psi_1|^2+|\Psi_2|^2)$, in which $\Gamma = 2\pi n_2/\lambda_0$ refers to the strength of the saturation parameter, with λ_0 the wavelength in free space. For a detailed derivation of the theoretical model, one may refer to Refs. [26,61]. Following the general settings, the total intensity of light can be calculated using the expression $I = \sum_{j=1}^{2}|\Psi_j|^2$. In Eq. (5), $\kappa = \pi n_{1R}/\lambda_0$ and $g = \pi n_{1I}/\lambda_0$ are the linear coupling coefficient and gain and loss profile of the fiber Bragg grating system, respectively. Based on the parameters g and κ, three distinct $\mathcal{PT}$-symmetric conditions can be formulated. For instance, when $g = \kappa$, we obtain a unique exceptional point (also known as the $\mathcal{PT}$-symmetric threshold level), while $g < \kappa$ leads to the broken-$\mathcal{PT}$-symmetric regime. Similarly, the condition $g > \kappa$ is known as the unbroken-$\mathcal{PT}$-symmetric regime as the system tends to show stable dynamics in this case [64]. Note that these classifications are utilized to describe the characteristic behavior of MI in four different domains, including the conventional case ($g = 0$) and below, at, and above the $\mathcal{PT}$-symmetric regimes for Eq. (5), in the present study.

Prior to performing a linear stability analysis of the proposed system (5), we wish to study the dispersion relations for both the conventional and $\mathcal{PT}$-symmetric cases. To this end, we consider the following counterpropagating cw solutions:

$$\Psi_1 = \alpha\exp[i(qz-\delta vt)], \tag{6a}$$

$$\Psi_2 = \beta\exp[i(qz-\delta vt)]. \tag{6b}$$

Here the parameters α and β indicate the forward and backward wave amplitudes that are assumed to be real constants, and the total power of the grating structure is defined as $\alpha^2 + \beta^2 = P$, which can also be calculated from $|\Psi_1|^2 + |\Psi_2|^2$. We now introduce a term that represents a ratio between the two constants as $f = \beta/\alpha$, where $\alpha = \sqrt{P/(1+f^2)}$ and $\beta = \sqrt{Pf^2/(1+f^2)}$. Substituting Eqs. (6) into the system (5), one can obtain a mathematical expression for nonlinear dispersion relations as given by

$$\delta = \frac{\Gamma}{(1+P)} - \frac{1}{2}\left(\frac{(\kappa+g)f^2+(\kappa-g)}{f}\right), \tag{7a}$$

$$q = \frac{(\kappa+g)f^2-\kappa+g}{2f}. \tag{7b}$$

Before studying the nonlinear dispersion relation, it is always instructive to first look into the characteristics of the linear dispersion relation, which can be obtained in the following way by turning off the saturable nonlinear parameter ($\Gamma = 0$) in Eq. (5), so that from Eq. (7), we have

$$\delta = -\frac{1}{2}\left(\frac{(\kappa+g)f^2+(\kappa-g)}{f}\right), \tag{8a}$$

$$q = \frac{(\kappa+g)f^2-\kappa+g}{2f}. \tag{8b}$$

By using Eqs. (8a) and (8b), the exact linear dispersion relation $\delta(q)$ can be found as

$$q^2 = \delta^2 - \kappa^2 + g^2. \tag{9}$$

Similarly, the exact nonlinear dispersion relation can be deduced as

$$q^2 = \left(\delta - \frac{\Gamma}{1+P}\right)^2 - \kappa^2 + g^2. \tag{10}$$

Figure 1 reveals the photonic band-gap structure as a result of the linear dispersion relation of the Bragg grating. As there exists a photonic band gap formed within a range of frequencies (which is also called forbidden frequencies), the propagation of light is restricted inside it, viz., between the upper and lower branches, and most of the light is reflected. Outside this region, light is allowed to traverse. Note that in a uniform medium without the presence of Bragg gratings, light propagates at its own speed. However, the inclusion of the Bragg grating exhibits a slowly decreasing dispersion at

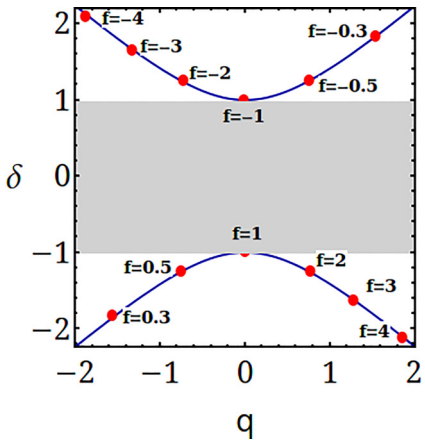

FIG. 1. Dispersion curve plotted between δ and q for the linear grating structure. Here $f = \mp 1$ refers to the top and bottom of the photonic band-gap structure with the system parameters $\kappa = 1$ and $g = 0$.

frequencies near the edges of the photonic band gap, where light experiences a slow propagation when compared to the uniform medium.

The parameter f is closely related to the group velocity in such a way that $v_g = d\delta/dq = [\kappa(1 - f^2) - g(1 + f^2)]/[\kappa(1 + f^2) - g(1 - f^2)]$. In particular, for $f = \pm 1$, the edges of the upper and lower branches of the dispersion curve are very close together and $f = -1$ and $f = 1$ are specified as the top and bottom of the photonic band gap, respectively. Also, when $f < 0$ it corresponds to the upper dispersion curve and the group velocity dispersion becomes negative, indicating the anomalous dispersion regime. On the other hand, $f > 0$ refers to the normal dispersion regime by the lower branch dispersion curve.

Based on Eq. (10), we present the characteristics of the nonlinear dispersion in Fig. 2 for the Bragg gratings under three different $\mathcal{PT}$-symmetric conditions with $P = 10$ and $\kappa = \Gamma = 1$. When $g = 0$, which refers to the conventional case, there is a typical propagation of forward and backward wave vectors, as shown in Fig. 2(a), with a broad band gap in which the formation of gap solitons would exist in the considered grating system. Upon increasing the value of g further ($g = 3$), i.e., below the $\mathcal{PT}$-symmetric threshold, one can observe that the size of the band gap has reduced considerably compared to the previous conventional case, as seen in Fig. 2(b). In contrast to the prior cases, no dispersion curve and band gap exist at the exceptional point (the $\mathcal{PT}$ threshold, $g = 5$), as seen in Fig. 2(c). Also, in this case, it is apparent that no localized structure, including gap solitons, can be observed. The role of the dispersion curve in the broken-$\mathcal{PT}$-symmetric regime is addressed in Fig. 2(d), where it can be clearly seen that the characteristics of the dispersion relation are similar to those of the regions such as conventional and below the $\mathcal{PT}$-symmetric threshold, except that the dynamics of the forward and backward wave vectors have been shifted clockwise by 90°. It is worth noting that the results corresponding to the nonlinear dispersion relations

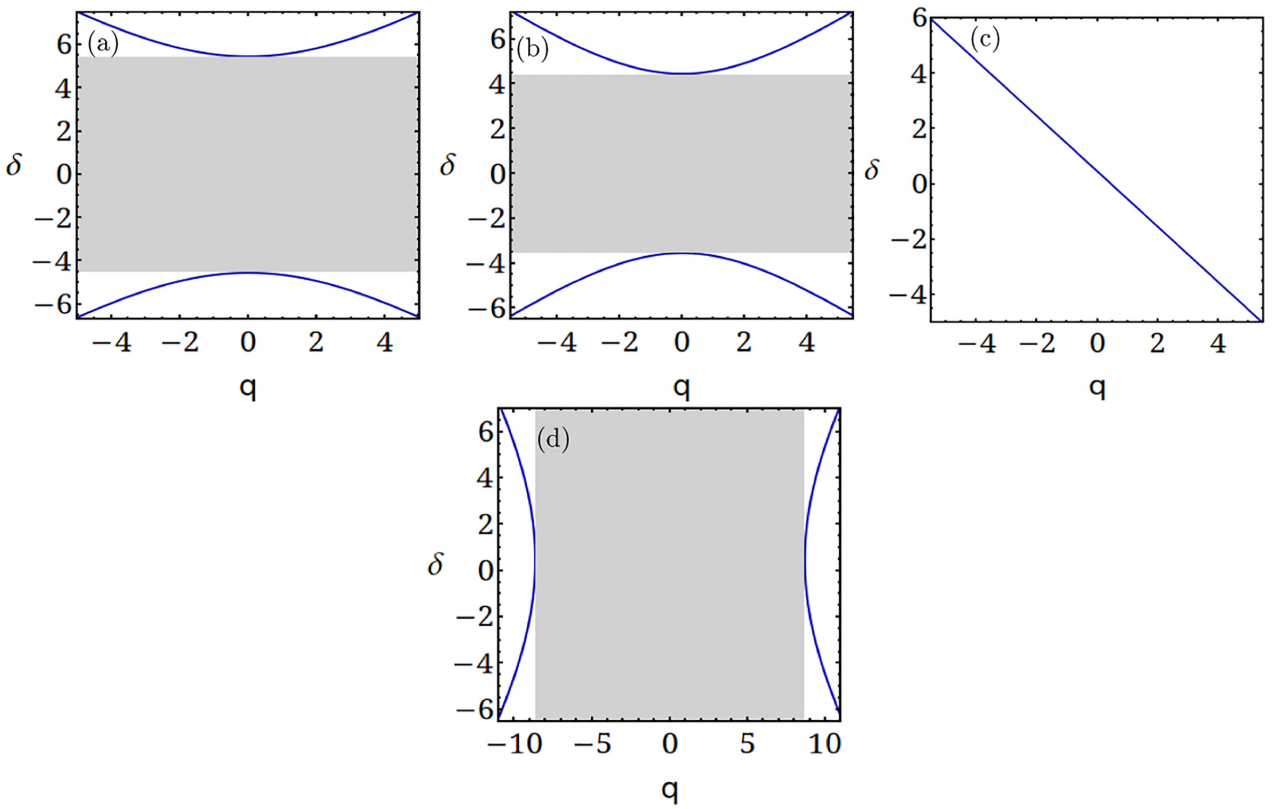

FIG. 2. Characteristics of the nonlinear dispersion relation drawn between δ and q for (a) the conventional case $g = 0$, (b) below the $\mathcal{PT}$-symmetric threshold $g = 3$, (c) at the $\mathcal{PT}$ symmetry $g = 5$, and (d) above the $\mathcal{PT}$-symmetric threshold $g = 10$. The rest of the parameters are $P = 10$ and $\kappa = \Gamma = 5$.

can be utilized to find Bragg and gap solitons in the nonlinear $\mathcal{PT}$-symmetric fiber Bragg gratings. Generally, the formation of a loop structure on either the upper or lower branches of a nonlinear dispersion curve is noticed in various types of periodic structures [52,53,65,66]. Nevertheless, the saturable $\mathcal{PT}$-symmetric FBG system under study never allows the formation of such a loop structure on the nonlinear dispersion curve due to the unique form of saturable nonlinearity considered here. In particular, the level of the nonlinearities (self-phase and cross-phase modulations) has been assigned with a ratio of 1:1 in the present system (5) as opposed to the 1:2 ratio, which is generally adopted in the Kerr-like Bragg grating structures [52,53,65,66]. As a result, this new ratio has changed the nonlinear dispersion relation in a way that the nonlinearity parameter Γ is present in Eq. (10) alone instead of appearing in both the dispersion relations, which in turn is one of the reasons for not supporting the formation of the loop in the dispersion curves.

For the investigation of the characteristic behavior of MI for the proposed system (5), we employ the standard method, namely, the linear stability analysis, in the next section.

III. LINEAR STABILITY ANALYSIS

In the linear stability analysis, infinitesimal perturbations are imposed on the cw state that result in the exponential growth of its amplitude. Based on the general procedure, let us consider the cw solutions (6) with small perturbations as follows:

$$\Psi_1 = [\alpha + a_1(z,t)]\exp[i(qz - \delta vt)], \tag{11a}$$

$$\Psi_2 = [\beta + a_2(z,t)]\exp[i(qz - \delta vt)]. \tag{11b}$$

The functions $|a_{1,2}|$ ($\ll\alpha, \beta$) are the perturbations imposed on the steady-state solution. Substituting Eq. (11) into Eq. (5) and linearizing with respect to the perturbations $a_{1,2}$, one can obtain the equations

$$ia_{1,z} + \frac{i}{v}a_{1,t} + \epsilon_1 a + \epsilon_2 a_2 + \epsilon(a_1^* + f a_2^*) = 0, \tag{12a}$$

$$-ia_{2,z} + \frac{i}{v}a_{2,t} + \epsilon_3 a_2 + \epsilon_4 a_1 + \epsilon(f a_1^* + f^2 a_2^*) = 0, \tag{12b}$$

where

$$\epsilon = \frac{\Gamma P}{(1+f^2)}, \quad \epsilon_1 = \epsilon - f(\kappa + g), \quad \epsilon_2 = \kappa + g + f\epsilon,$$
$$\epsilon_3 = \frac{g-\kappa}{f} + f^2\epsilon, \quad \epsilon_4 = f\epsilon + (\kappa - g). \tag{13}$$

Next we consider the Fourier components of the perturbed cw amplitudes $a_{1,2}(z,t)$ as

$$a_1(z,t) = p_+ e^{i(Kz-\Omega t)} + p_- e^{-i(Kz-\Omega t)}, \tag{14a}$$

$$a_2(z,t) = q_+ e^{i(Kz-\Omega t)} + q_- e^{-i(Kz-\Omega t)}. \tag{14b}$$

Here p_+ and q_+ represent the forward propagation, whereas p_- and q_- represent the backward propagation. Also, K and Ω indicate the wave number and frequency of the perturbation, respectively. In what follows, on the basis of the terminology adopted in the study of light scattering in quantum mechanics [67], we will refer to the region in which the wave number takes negative values ($K < 0$) as the Stokes wave-number region and the other region in which the wave number is positive ($K > 0$) is known as the anti-Stoke wave-number region [68]. Substituting the above solutions (14a) and (14b) into the governing equations (5) and linearizing the resultant equations with the perturbed amplitudes p_+ and p_- and q_+ and q_-, one obtains four homogeneous equations in the matrix form

$$[Y] \times [u]^T = 0, \quad u^T = (p_+, q_+, p_-, q_-), \tag{15}$$

where Y is a 4×4 matrix with the elements

$$y_{11} = -f(\kappa + g) - K + \epsilon + \Omega, \quad y_{12} = \epsilon,$$
$$y_{13} = \kappa + g + f\epsilon, y_{14} = f\epsilon, \quad y_{21} = \epsilon,$$
$$y_{22} = -f(\kappa + g) + K + \epsilon - \Omega, \quad y_{23} = f\epsilon,$$
$$y_{24} = g + \kappa + f\epsilon,$$
$$y_{33} = (g-\kappa)/f + K + f^2\epsilon - +\Omega, \quad y_{31} = \kappa - g + f\epsilon,$$
$$y_{32} = f\epsilon, \quad y_{34} = f^2\epsilon, \quad y_{41} = f\epsilon, \quad y_{43} = f^2\epsilon,$$
$$y_{42} = \kappa - g + f\epsilon, \quad y_{44} = (g-\kappa)/f - K + f^2\epsilon - \Omega. \tag{16}$$

It is important to note that the Y matrix has nontrivial solutions when its determinant vanishes, which in turn leads to the quartic polynomial equation in Ω,

$$\Omega^4 + a\Omega^2 + b\Omega + c = 0, \tag{17}$$

where

$$a = -\frac{K^2 d_2 g^2 + 2e_1 g\kappa + \kappa^2 + f^4\kappa^2 + 2f^2 e_3}{f^2},$$
$$b = -\frac{2Ke_1 g^2 + e_1\kappa^2 + 2g(-2f^3\epsilon + \kappa + f^4\kappa)}{f^2},$$
$$c = -\frac{d_1 g^2 + 2e_1 g\kappa - 2f^3\epsilon\kappa + \kappa^2 + f^4\kappa^2 - f^2 e_2}{f^2},$$
$$d_{1,2} = (\pm 1 + f^2)^2, \quad e_1 = (-1 + f^4),$$
$$e_2 = [K^2 + 2\kappa(3f\epsilon + \kappa)], \quad e_3 = (K^2 + \kappa^2). \tag{18}$$

This quartic polynomial equation has four branches of the solution when $\Omega(K)$ satisfies the relations

$$\Omega_{1-4} = \pm\frac{1}{2\sqrt{6}}[\sqrt{\mathrm{sgn}(\nu_1)|\nu_1|} \pm \sqrt{\mathrm{sgn}(\nu_2)|\nu_2|}], \tag{19}$$

where

$$\nu_1 = -4a + \frac{\Upsilon_1}{\Upsilon_2} + 2^{(2/3)}\Upsilon_2,$$
$$\nu_2 = -8a - \frac{\Upsilon_1}{\Upsilon_2} - 2^{(2/3)}\Upsilon_2 \pm \frac{12 \times \sqrt{6}b}{\sqrt{\nu_1}},$$
$$\Upsilon_1 = 2 \times 2^{(1/3)}(a^2 + 12c),$$
$$\Upsilon_2 = (2a^3 + 27b^2 - 72ac + \eta)^{(1/3)},$$
$$\eta = \sqrt{-4(a^2 + 12c)^3 + (2a^3 + 27b^2 - 72ac)^2}. \tag{20}$$

Note that one can find the conditions for which the four branches of the above relation given in Eq. (19) become imaginary, which include (i) $\mathrm{sgn}(\nu_1) < 0$ and $\mathrm{sgn}(\nu_2) < 0$, (ii) $\mathrm{sgn}(\nu_1) > 0$ and $\mathrm{sgn}(\nu_2) < 0$, and (iii) $\mathrm{sgn}(\nu_1) < 0$ and $\mathrm{sgn}(\nu_2) > 0$. Hence the growth rate of the MI gain spectrum $G(K)$ can be calculated using the relation $G(K) = \mathrm{Im}(\Omega_{\max})$,

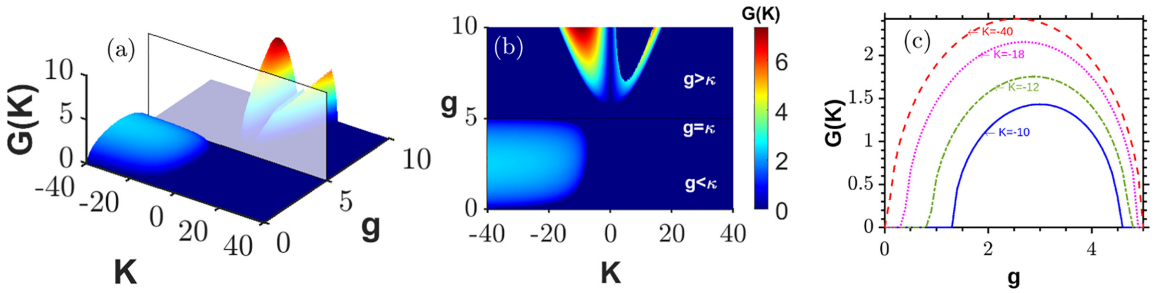

FIG. 3. (a) MI gain spectra with the variation in g at the bottom of the photonic band gap $f = 1$, (b) its corresponding contour view, and (c) peak gain of the peculiar MI spectrum as a function of the gain or loss parameter for different values of the wave number. The other parameters are $\kappa = 5$, $P = 1$, and $\Gamma = 5$.

where Ω_{max} represents the largest imaginary part of the four branches. The purpose of this study is to examine the dynamics of cw instability in the two different dispersion regimes, namely, the anomalous dispersion regime ($f < 0$) and the normal dispersion regime ($f > 0$). As a first step, we examine the MI gain spectrum emerging at the bottom and top of the photonic band gaps. We will also analyze how the various system parameters, such as gain or loss, the saturable nonlinear coefficient, and power, influence the MI spectrum in each of the $\mathcal{PT}$-symmetric domains.

IV. INVESTIGATION Of MODULATIONAL INSTABILITY

A. Bottom of the photonic band gap

We investigate here the MI gain spectrum as a function of the gain and loss parameter g at the bottom of the photonic band gap ($f = 1$). When the value of the linear coupling coefficient is fixed at $\kappa = 5$, the resultant MI gain spectrum is illustrated for the continuous variation of g invoking all three $\mathcal{PT}$-symmetric regimes in addition to the conventional case. The results are shown in Figs. 3(a) and 3(b), where one can observe a peculiar spectrum for a certain range of g ($0 < g < 4.9$) on only one side (left) of the zero value of perturbation wave number, while on the other side the system does not experience any instability at all by exhibiting no sideband there even after the addition of the perturbation with a wide range of input wavelengths. It is pertinent to note that the spectrum obtained in the unbroken-$\mathcal{PT}$-symmetric regime is unique in two aspects when compared to the standard spectrum obtained in conventional systems. First, although the growth rate of cw instability tends to rise gradually with an increase in the value of wave number, the exponential growth is predominantly noticed as a function of the gain or loss parameter, which is clearly seen in Fig. 3(c). Second, the shape of the MI spectrum is different as the exponential growth is observed with the increase in the value of the gain or loss parameter with a peak gain in the middle of these values in contrast to the perturbation wave number. We would like to emphasize that the finding of such a spectrum has not been reported in any conventional and $\mathcal{PT}$-symmetric FBGs. With a further increase in g leading to the broken-$\mathcal{PT}$-symmetric regime, it is quite interesting to observe the conventional MI gain spectrum (as obtained in the standard nonlinear Schrödinger equation in the *anomalous dispersion regime*) appearing on either side of the perturbation wave number K for a certain (minimum) range of gain or loss parameter g ($5.8 < g < 7$). Nevertheless, subsequently, it turns out to be a case of two distinct sidebands (asymmetric spectra) that include a huge gain spectrum with a wide bandwidth that appeared in the Stokes wave-number region while a split occurs in the MI spectrum on the other side which eventually leads to two different additional spectra, including the primary one found near the zero-perturbation wave number with a lower gain and bandwidth and a secondary MI band which is far detuned with a higher gain and bandwidth.

To gain further insight into the characteristic behavior of the instability spectra obtained at the bottom of the photonic band gap, we present two additional plots in Fig. 4 that delineate the MI growth rates as a function of g for two different values of the saturable nonlinearity, including $\Gamma = 6$ and 10. From Fig. 4(a) it is clear that the structure of the MI spectrum changes differently as a result of tuning the parameter g from the conventional case to different $\mathcal{PT}$-symmetric regimes. As pointed out earlier, here too we notice the peculiar MI spectrum in the unbroken-$\mathcal{PT}$-symmetric regime. Upon reaching the $\mathcal{PT}$-symmetric threshold condition, there are two different sidebands that got split up from the conventional one: the primary MI spectrum located further in the Stokes wave-number regime and a secondary MI spectrum in the positive wave-number region having a lower gain compared to the former. The gain and bandwidth of MI spectra are dramatically enhanced by one-third as much as in the former case when we increase the value of g further ($g = 15$). Furthermore, when we set the value of the nonlinear saturable parameter at $\Gamma = 10$ [see Fig. 4(b)], we observe a slightly modified MI gain spectrum compared to the previous one for each value of g. For example, the peculiar spectrum appears in the anti-Stokes wave-number region too for $g = 1$. Similarly, the MI band observed in the Stokes wave-number region is

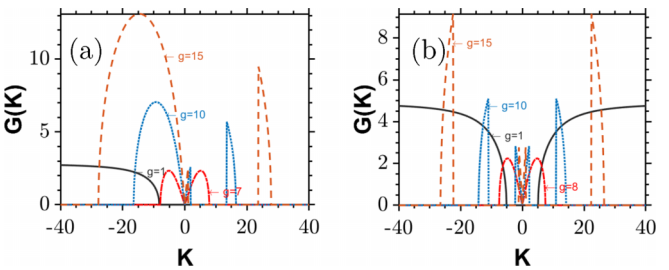

FIG. 4. One-dimensional MI spectra for different values of g for (a) $\Gamma = 6$ and (b) $\Gamma = 10$. The parameters are $\kappa = 5$ and $P = f = 1$.

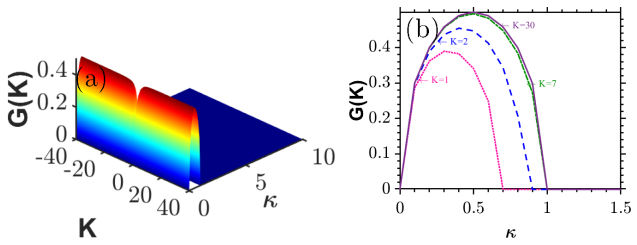

FIG. 5. (a) MI gain spectra as a function of κ at the bottom of the photonic band gap $f = 1$ for the conventional case ($g = 0$). (b) Maximum gain of a peculiar MI spectrum versus the coupling coefficient κ for distinct wave numbers. Here the parameters are $P = 1$ and $\Gamma = 1$.

also split up into two different bands as noticed in the previous case, as shown in Fig. 4(a). In addition, the values of gain and bandwidth are significantly suppressed at each g value relative to the previous case. These ramifications clearly reveal the fact that the role of saturable nonlinearity is intense in altering the MI spectrum in the presence of the gain or loss parameter.

1. Impact of the coupling coefficient κ

We now investigate the role of the coupling coefficient κ in the development of the MI gain spectrum at the bottom of the photonic band gap ($f = 1$) as shown in Fig. 5(a). Note that we present here only the conventional case by setting the gain or loss parameter to zero, since the different $\mathcal{PT}$-symmetric conditions exhibit the same MI pattern as witnessed in Fig. 4 when we tune the value of gain or loss parameter. Now arriving at the conventional system, the role of the coupling parameter results in the peculiar MI spectrum appearing on either side of the perturbation wave number K in the range $0 < \kappa < 1$. By further increasing the value of κ, it is apparent that the cw exhibits complete stable propagation on both sides of the wave number without exhibiting any instability. Also, in light of this investigation, it can easily be interpreted that the cw propagation is unstable whenever the coupling coefficient κ has a nontrivial value (up to unity in the normalized scale) in the conventional system for the given system parameters. Also note that the maximum MI gain of the peculiar spectrum significantly increases as the wave number K increases, though the spectrum is obtained as a function of the coupling coefficient as seen in Fig. 5(b).

2. Impact of power

This section examines how power affects the MI gain spectrum at the bottom of the photonic band gap. As can be seen in Fig. 6(a), in the conventional case ($g = 0$), a symmetric pattern of monotonically increasing side gain emerges on either side of the central perturbation wave number ($K = 0$), which appears to become wider with an increase in the value of P. There is also a significant separation distance between the monotonically increasing side gains. These symmetric MI patterns can be turned into asymmetric ones as shown in Fig. 6(b) by tuning the value of g to $g = 3$, i.e., below the $\mathcal{PT}$-symmetric threshold. Also, the increase in the value of g results in a suppression of the monotonically increasing side gain located in the Stokes wave-number region, thereby

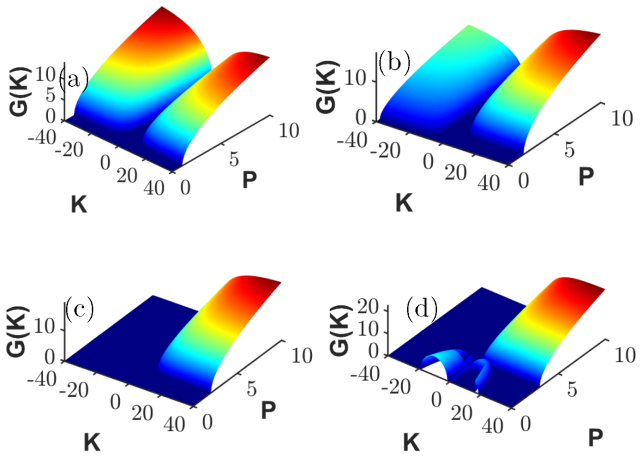

FIG. 6. MI gain spectra as a function of P at the bottom of the photonic band gap $f = 1$ for four different cases: (a) conventional, (b) below, (c) at, and (d) above $\mathcal{PT}$-symmetric thresholds. The parameters are $\kappa = 5$, $\Gamma = 5$, and $f = 1$.

leading to a drop in its growth rate from that of the side gain in the anti-Stokes wave-number region. At the $\mathcal{PT}$-symmetric threshold regime [see Fig. 6(c)], monotonically increasing the side gain in the Stokes wave-number region gets completely suppressed and the cw exhibits stable dynamics, whereas the side gain located in the anti-Stokes wave-number region remains the same against the variation in P. Note that in all of the above situations, the side MI gain increases as the input power increases. In the case of the broken-$\mathcal{PT}$-symmetric regime, the MI spectrum qualitatively changes into an unusual one featuring two asymmetric MI sidebands on either side of the zero-perturbation wave number as seen in Fig. 6(d). In particular, one can observe a huge MI gain spectrum with a wide bandwidth in the Stokes wave-number region and a set of two distinct spectra that include the primary MI sideband and secondary MI band in the anti-Stokes wave-number region. With a small increase of P, these MI spectra tend to split on the side of the Stokes wave number and try to merge together on the other side. A further increment in the value of P combines all the former spectra into a single huge spectrum with a monotonically increasing side gain in the anti-Stokes wave-number region.

3. MI as a function of saturable nonlinearity

In this section we analyze the impact of the nonlinear parameter Γ on the development of the MI gain spectrum at the bottom of the photonic band gap, as presented in Fig. 7 with constant values of P and κ for four different cases of the $\mathcal{PT}$-symmetric system. For the conventional case, the instability spectrum as a function of Γ can be seen in Fig. 7(a). Here the monotonically increasing side gains are visible on either side of the zero wave number, where the peak gain rises with an increase in the Γ parameter. On the other hand, in the unbroken $\mathcal{PT}$-symmetric regime, as shown in Fig. 7(b), there exist the asymmetric MI spectra, while in the $\mathcal{PT}$-symmetric threshold regime a single monotonically increasing side gain arises in the anti-Stokes wave-number region [Fig. 7(c)]. Note that in both cases too, the growth rate tends to increase as the

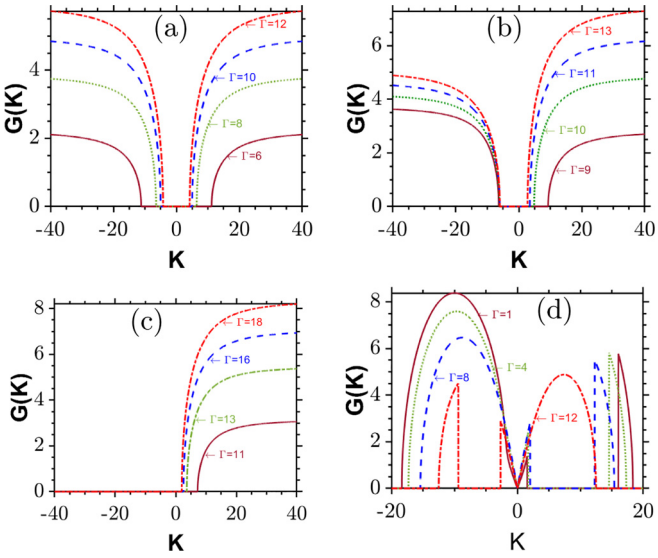

FIG. 7. Development of instability gain spectra with the variation of the nonlinear parameter Γ at the top of the photonic band gap $f = 1$ for four different cases: (a) conventional, (b) below, (c) at, and (d) above $\mathcal{PT}$-symmetric thresholds. The parameters are $\kappa = 5$, $P = 1$, and $f = 1$.

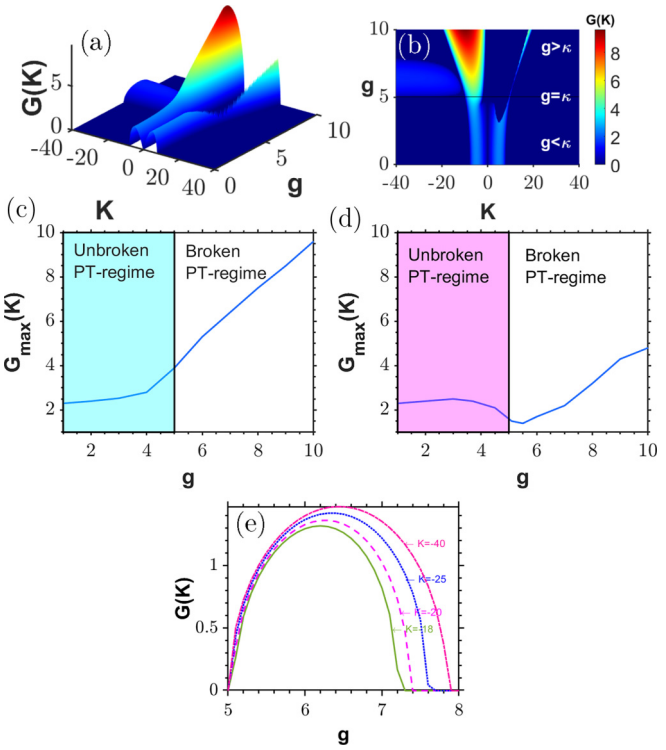

FIG. 8. (a) MI gain spectra as a function of g at the top of the photonic band gap $f = -1$. (b) Corresponding contour plot. The maximum gains of the MI spectra obtained in the (c) Stokes and (d) anti-Stokes wave-number regions are illustrated for the variation in g. (e) Peculiar MI spectrum versus the gain or loss parameter g for different wave numbers. The parameters are $\kappa = 5$, $P = 1$, and $\Gamma = 3$.

nonlinear saturable parameter is increased. On the other hand, the broken-$\mathcal{PT}$-symmetric regime [see Fig. 7(d)] reveals two distinct MI gain spectra on either side of the zero wave number ($K = 0$), in which the gain and bandwidth increase as Γ is decreased, in contrast to the previous cases. Here, interestingly, when the saturation parameter is increased to $\Gamma = 12$ (red dash-dotted sideband), the dramatic dynamics of MI is observed where the spectra become completely shifted from the Stokes to the anti-Stokes wave-number region and vice versa.

B. Instability at the top of the photonic band gap

In this section we explore the dynamics of instability at the top of the photonic band gap ($f = -1$), where the gain or loss parameter g is assumed to vary continuously while the other parameters such as power, κ, and Γ are kept constant. The instability spectrum for the top of the photonic gap is shown in Fig. 8(a) and its corresponding contour diagram is plotted in Fig. 8(b). Here the MI gain spectrum primarily overlaps with the conventional MI gain spectrum (as obtained in the standard nonlinear Schrödinger equation in the anomalous dispersion regime) appearing on either side of the zero-perturbation wave number ($K = 0$) in the unbroken-$\mathcal{PT}$-symmetric regime and it continues to exhibit similar features near the $\mathcal{PT}$-symmetric threshold region (i.e., $0 < g < 4.8$). Note that in this case the MI peak gain and bandwidth increase moderately with an increase in the value of g on both sides of the anti-Stokes and Stokes wave number until it reaches the $\mathcal{PT}$-symmetric threshold. As the value of g increases further, which translates the system into the broken-$\mathcal{PT}$-symmetric regime, there is an emergence of a huge MI gain spectrum with a wide bandwidth in the Stokes wave-number region, while a narrow sideband emerges in the anti-Stokes wave-number region. Specifically, the MI spectrum found in the Stokes wave-number region has a gain that is three times greater than the other spectrum observed in the anti-Stokes wave-number region. Another notable ramification is the formation of a peculiar MI gain spectrum in the Stokes wave-number region which is perpendicular to the huge primary MI spectrum. There is an increase in the value of MI gain and the bandwidth of the former as the value of K increases in the negative direction. For further understanding, we separately present the growth rate of the MI gain spectrum obtained in the Stokes and anti-Stokes wave-number regions in Figs. 8(c) and 8(d), respectively, where we observe that peak gain significantly increases when the gain or loss parameter varies from the unbroken-$\mathcal{PT}$-symmetric regime to the broken-$\mathcal{PT}$-symmetric regime. Following that, we present the maximum gain of the peculiar MI spectrum obtained in the Stokes wave-number region for different values of the wave number K in Fig. 8(e). In this case, needless to say, the maximum MI gain of the peculiar spectrum is significantly increased with increasing wave number K besides an increase in g.

1. Role of the coupling coefficient κ

We next study the MI dynamics as a function of the coupling coefficient κ at the top of the photonic band gap ($f = -1$), where all other parameters such as the gain or loss parameter g, the power P, and nonlinearity coefficient Γ are

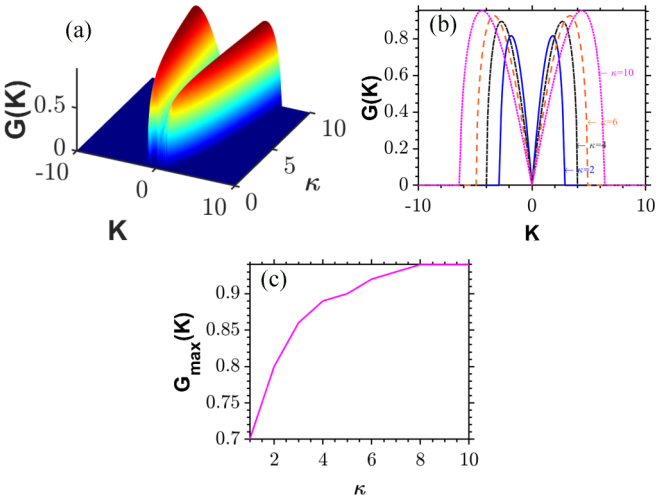

FIG. 9. (a) Role of the coupling coefficient in the MI gain spectra at the top of the photonic band gap $f = -1$ for the conventional case. (b) Corresponding one-dimensional plot. (c) Maximum gain of the MI spectra versus κ in the Stokes wave-number region. The other parameters are $P = 1$ and $\Gamma = 1$.

kept constant with the values $P = \Gamma = 1$. The conventional case is only shown here by setting $g = 0$; see Fig. 9, where one can clearly notice that the system is stable until the value of κ attains unity. Upon increasing the value of κ, a typical MI gain spectrum appears on either side of the zero-perturbation wave number ($K = 0$), where the gain and bandwidth of the spectrum are enhanced by increasing the value of κ further, which is then corroborated in Fig. 9(c).

2. Role of power

To analyze the role of power at the top of the photonic band gap, we keep the values of κ and Γ as $\kappa = 5$ and $\Gamma = 3$ with a variation in the value of g that corresponds to different $\mathcal{PT}$-symmetric regimes. Figure 10(a) shows the conventional case,

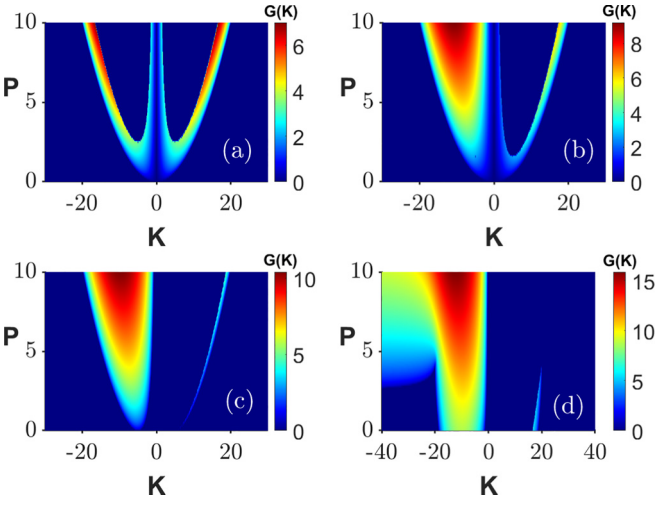

FIG. 10. Impact of the power on the instability spectra in the top of the photonic band gap for (a) conventional, (b) below, (c) at, and (d) above $\mathcal{PT}$-symmetric thresholds. The parameters are $\kappa = 5$, $\Gamma = 2$, and $f = -1$.

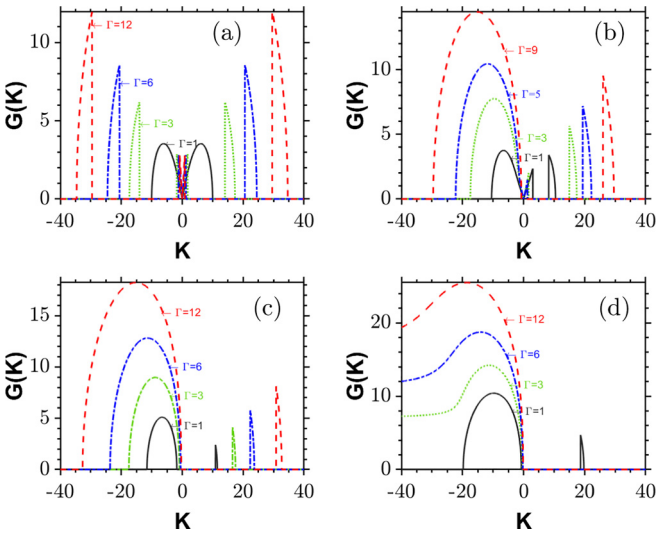

FIG. 11. Role of the nonlinear Γ parameter on the MI gain spectra in the top photonic band gap for (a) conventional, (b) below, (c) at, and (d) above the $\mathcal{PT}$-symmetric threshold. The parameters are $\kappa = 5$, $P = 5$, and $f = -1$.

where the MI gain spectrum evolves primarily as a typical MI gain spectrum on the two sides of the wave number. However, after a particular value of power ($P > 2.7$), the MI sidebands begin to break into primary and secondary MI bands in both the Stokes and anti-Stokes wave-number regions. In both spectra, the gain and bandwidth of the secondary sideband are approximately twice that of the primary sidebands and the dynamics persist even after a further increase in P. It is worth mentioning that the structure of these MI spectra seems to have a shape of υ. In the unbroken-$\mathcal{PT}$-symmetric regime [see Fig. 10(b)], the previous υ-shaped spectrum transforms into a complete single spectrum (without revealing any discreteness in the spectrum) in the Stokes wave-number region, while its counterpart remains unchanged, as seen in Fig. 10(a). The impact of the power in the $\mathcal{PT}$-symmetric threshold region is depicted in Fig. 10(c). In this case, the MI spectrum in the Stokes wave-number region gets enhanced moderately in both its gain and width. On the other hand, the spectrum observed in the anti-Stokes wave-number region is drastically suppressed, revealing a very thin bandwidth. In the broken-$\mathcal{PT}$-symmetric regime [see Fig. 10(d)], when the value of P is low, there exists an emergence of the typical spectrum after which one can observe the emergence of an additional peculiar MI gain spectrum in the Stokes wave-number region with an increase in the value of P ($P > 3.5$). On the other hand, the sideband on the anti-Stokes wave-number region almost disappears compared to the previous case. Note that in all of the above four cases, a common increase in the gain and bandwidth of the MI spectra is clearly visible as the value of P increases.

3. Impact of the nonlinear parameter Γ

We now examine the impact of the nonlinear parameter Γ at the top of the photonic band gap in different regimes of $\mathcal{PT}$ symmetry. These results are shown in Fig. 11, with fixed values of the system parameters P and κ. In the conventional

case, the spectrum primarily exhibits a typical MI gain spectrum for the low value of the nonlinear parameter ($\Gamma = 1$), as shown in Fig. 11(a). However, as Γ increases, the secondary MI spectrum starts to emerge followed by the former primary MI gain on either side of the zero wave number. In addition, as the value of Γ increases, the spectrum gets enhanced and the separation distance between the primary and secondary MI bands also increases by shifting towards the higher wave number. We then analyze the MI dynamics in the unbroken-$\mathcal{PT}$-symmetric regime, which is illustrated in Fig. 11(b). Here it is obvious that the system exhibits asymmetric MI gain spectra on both sides of the wave number, including a huge primary MI spectrum in the Stokes wave-number region while its counterparts remain almost unchanged except for $\Gamma = 1$ as in Fig. 11(a). Further, it can be seen in Fig. 11(c) that the MI gain spectrum retains the same dynamics even when moving to the $\mathcal{PT}$-symmetric threshold regime. Nevertheless, for each nonlinear saturation parameter value, the peak gain of the sidebands in the Stokes wave-number region increases moderately compared to the previous cases shown in Figs. 11(a) and 11(b); however, the gain in the sidebands on the other side falls as the value of Γ increases. In the broken-$\mathcal{PT}$-symmetric regime, the sidebands become a monotonically increasing gain in the Stokes wave-number region, while the other side displays the stable dynamics of the cw state except for $\Gamma = 1$, as shown Fig. 11(d).

C. Modulational instability in the anomalous dispersion regime

Another significant part of this study is to investigate the dynamics of MI in the anomalous dispersion regime of the proposed system (5). As studied in the previous sections, we also investigate here the emergence of the MI gain spectrum in three $\mathcal{PT}$-symmetric regimes, besides the conventional case. Also, we investigate the MI gain spectrum for four different dispersion parameter values in the anomalous dispersion regime. Compared to the earlier results presented in the paper, all of these cases give rise to various unique MI gain spectra. For instance, in the unbroken-$\mathcal{PT}$-symmetric regime, two different MI sidebands can be observed when the value of f is fixed at $f = -0.1$ [see Fig. 12(a)]. Note that the MI sideband located in the anti-Stokes wave-number region side is slightly larger in gain and wider in bandwidth compared to the spectrum that appeared on the other side. It is also observed that an additional secondary MI spectrum emerges closer to the MI sideband in the Stokes wave-number region. When we increase the value of the gain or loss parameter further, in particular, towards the $\mathcal{PT}$-symmetric threshold, all these MI spectra tend to merge in the Stokes wave-number region and disappear in the anti-Stokes wave-number region due to the presence of singularity. In the broken-$\mathcal{PT}$-symmetric threshold regime, one can notice the magnified mirror image of the MI gain spectrum found in the unbroken-$\mathcal{PT}$-symmetric regime. However, the gain and bandwidth of the MI spectrum are significantly enhanced in this case compared to the unbroken regime.

Figure 12(b) shows the MI gain spectrum as a function of g by fixing the dispersion parameter as $f = -0.5$. In this case, the patterns of these MI sidebands seem to be more complicated than the previous one with some irregularities

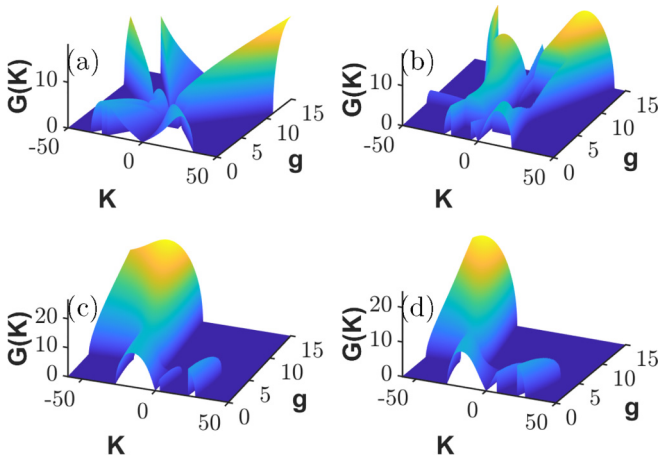

FIG. 12. Instability gain spectra in the anomalous dispersion regime as a function of g for different dispersion values: (a) $f = -0.1$, (b) $f = -0.3$, (c) $f = -3$, and (d) $f = -5$. The other parameters are $P = 10$, $\kappa = 5$, and $\Gamma = 3$.

in all the $\mathcal{PT}$-symmetric regimes. To elucidate the dynamics further, it is apparent that most of the MI dynamics resemble the previous spectra except for the emergence of an additional peculiar MI spectrum parallel to the primary MI spectrum formed in the Stokes wave-number region. This spectrum continues to extend as the wave number increases. By further decreasing the value of the dispersion parameter to $f = -3$, it becomes evident that the dynamics of the MI gain spectrum, portrayed in Fig. 12(c), is significantly simpler than in the previously studied cases [cf. Figs. 12(a) and 12(b)]. There are two distinct MI sidebands, where the gain of the MI sideband in the Stokes wave-number region is higher than the spectrum in the anti-Stokes wave-number region. Additionally, a secondary MI band can be observed in the anti-Stokes wave-number region with a higher MI gain than the primary MI spectrum. Upon increasing the value of g further, the MI sideband in the Stokes wave-number region transforms into a pronounced monotonically increasing gain. The structure of the MI spectrum remains the same when the dispersion parameter is further decreased to $f = -5$, as illustrated in Fig. 12(d). However, the gain of the primary and secondary MI bands is significantly enhanced from the spectra obtained when $f = -3$.

1. Influence of κ on the MI gain spectrum

Figure 13 shows the impact of the coupling coefficient κ on the formation of MI gain spectrum in the anomalous dispersion regime for $f = -0.1$ in the conventional case alone. For this purpose, we continuously change the coupling coefficient κ while maintaining constant values for the gain or loss parameter, power, and saturable nonlinear parameter. As in the previous case, shown in Fig. 9(a), here too, a typical MI gain spectrum is observed which further extends on either side of the zero-perturbation wave number as the coupling coefficient varies. When κ is increased, the MI gain and bandwidth of the spectrum are significantly increased in the anti-Stokes and Stokes wave-number regions, which is further corroborated in Fig. 9(b).

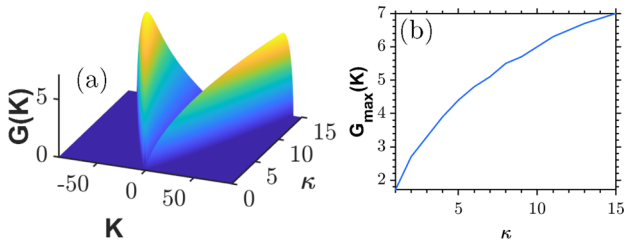

FIG. 13. (a) MI gain spectra as a function of κ for the anomalous dispersion regime. (b) Maximum gain of the peculiar spectra versus κ in the Stokes wave-number region. The parameters are $g = 0$, $\Gamma = 1$, $P = 10$, and $f = -0.1$.

2. *Influence of input power P*

The role of input power in the anomalous dispersion regime has also been analyzed in greater detail for all the $\mathcal{PT}$-symmetric threshold regimes as well as the conventional case. Figure 14(a) delineates the MI gain spectrum for the conventional case as a function of power. Here the typical MI gain spectrum is observed around the zero-perturbation wave number and the values of gain and bandwidth become more pronounced by further increasing the value of P. In particular, one can witness a small range of irregularities due to the singularity arising in the Stokes wave-number region. The same MI structure remains almost unchanged qualitatively when the system is operated in the unbroken-$\mathcal{PT}$-symmetric regime [see Fig. 14(b)]. However, the gain and bandwidth of the MI spectrum are somewhat reduced and the range of irregularities that appear in the Stokes wave-number region is extended. The scenario has been changed when switching to the $\mathcal{PT}$-symmetric threshold regime, where one can observe the manifestation of asymmetric MI gain spectra that include the typical MI spectrum in the Stokes wave-number region and a very narrow sideband in the anti-Stokes wave-number region, as shown in Fig. 14(c). In this case

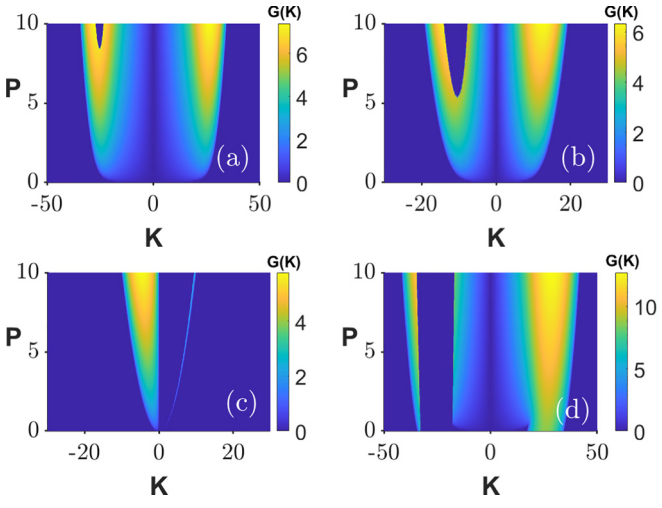

FIG. 14. MI gain spectra in the anomalous dispersion regime as a function of P for (a) conventional, (b) below, (c) at, and (d) above $\mathcal{PT}$-symmetric thresholds. The parameters are $\kappa = 5$, $\Gamma = 3$, and $f = -0.1$.

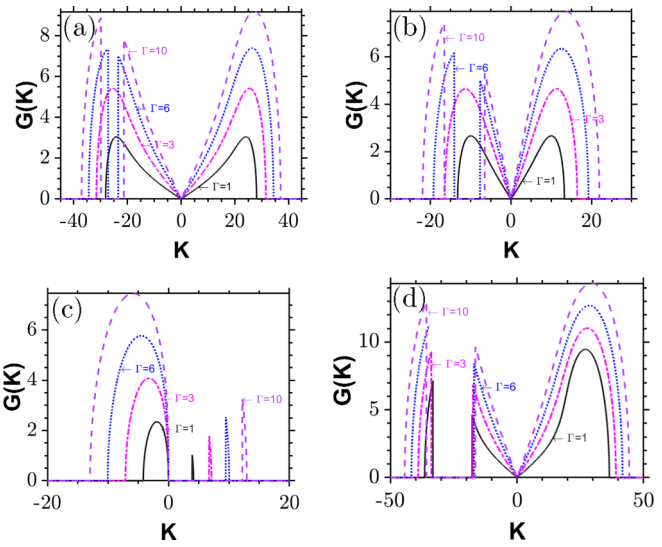

FIG. 15. MI gain spectra as a function of Γ in the anomalous dispersion regime for (a) conventional, (b) below, (c) at, and (d) above $\mathcal{PT}$-symmetric thresholds for $f = -0.1$ and $\kappa = P = 5$.

too the MI gain increases with the increase in the value of P. In the broken-$\mathcal{PT}$-symmetric regime [see Fig. 14(d)] there exist two asymmetric MI spectra, which include a wider MI spectrum in the anti-Stokes wave-number region and two different MI sidebands in the Stokes wave-number side.

3. *Impact of the nonlinear saturation parameter* Γ

We now investigate the influence of the nonlinear saturation parameter on the instability spectrum in the anomalous dispersion regime under three different $\mathcal{PT}$-symmetric conditions with the conventional case. Figure 15(a) shows the MI dynamics in the conventional case where a symmetric MI spectrum is observed on both sides of the wave number. However, when the value of the saturation parameter is increased to $\Gamma = 6$, the spectrum becomes asymmetric, wherein two different MI bands start to appear. Also, the MI gain and bandwidth of both the primary and secondary MI gain spectra increase as the value of Γ increases. When the system is operated in the unbroken regime [see Fig. 15(b)], though the MI spectrum seems to overlap with the conventional case for lower values of Γ, a further increase in the value of Γ, for instance, $\Gamma = 6$, transforms the symmetric spectrum into an asymmetric one. What differentiates this from the former is that the spectrum results in a slightly narrower bandwidth and lower gain compared to the conventional case. The exceptional point, shown in Fig. 15(c), reveals a different MI spectrum where very thin and lower gain MI peaks emerge in the anti-Stokes wave-number region, while on the other side the spectrum features a wider bandwidth and higher gain. Finally, in the broken-$\mathcal{PT}$-symmetric case as illustrated in Fig. 15(d), it retains the same MI patterns obtained in both the conventional and unbroken-$\mathcal{PT}$-symmetric cases. Nevertheless, the separation distance between the primary and secondary MI bands is much higher in the Stokes wave-number region, while the

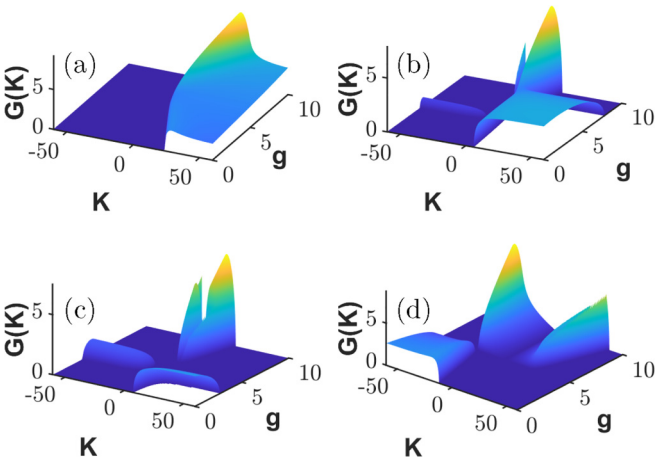

FIG. 16. MI gain spectra as a function of the gain or loss parameter in the normal dispersion regime for different f values: (a) $f = 0.1$, (b) $f = 0.5$, (c) $f = 0.7$, and (d) $f = 5$. The other parameters are $\kappa = 5$ and $P = \Gamma = 2$.

spectrum in the anti-Stokes wave-number region exhibits a much wider bandwidth.

D. Modulational instability in the normal dispersion regime

This section presents another important study of the MI spectrum obtained in the normal dispersion regime ($f > 0$). For this reason, all the parameters except g are fixed and, like in the preceding section, we present the investigation by assigning different values of the dispersion parameter f by continuously varying the gain or loss parameter. The MI gain spectrum is shown in Fig. 16(a) as a function of g when the value of f is set to a low value, such as $f = 0.1$. Unlike in the anomalous dispersion regime, here the MI spectrum takes place only in the anti-Stokes wave-number region and on further increasing the value of gain or loss coefficient, the spectrum drifts towards the zero-perturbation wave number with a magnitude drop in its gain. Near the broken-$\mathcal{PT}$-symmetric region, the MI spectrum in the anti-Stokes wave-number region drifts again in the opposite direction.

Upon further increasing the value of f to 0.5 ($f = 0.5$) [Fig. 16(b)], a unique MI gain spectrum is observed. The spectrum primarily appears with a monotonically increasing sideband gain in the anti-Stokes wave-number region. In parallel, a peculiar MI gain spectrum can be seen in the Stokes wave-number region, which is enhanced further as K increases. Once the system reaches the broken-$\mathcal{PT}$-symmetry regime, the monotonically increasing MI side gain transforms into two distinct primary MI spectra around $K = 0$, with the MI sideband in the anti-Stokes wave-number regime being more prominent than the MI sideband on the other side, whose gain and bandwidth increase with increasing g values. We notice that the scenario changes a bit when we assign the value of f as $f = 0.7$. This increase in the value of the dispersion parameter separates the monotonically increasing spectrum from the primary MI spectrum in the anti-Stokes wave-number regime, as shown in Fig. 16(c). Also, the peculiar MI spectrum in the negative wave-number region is significantly enhanced compared to the previous case [see Fig. 16(b)]. In contrast

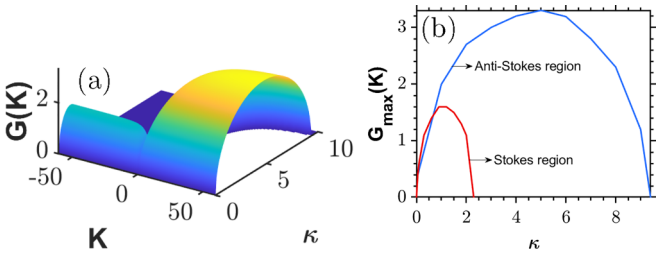

FIG. 17. (a) MI gain spectra as a function of the coupling coefficient κ in the normal dispersion regime. (b) Maximum gain of the peculiar MI gain as a function of coupling coefficient κ. The parameters are $g = 0$, $P = 5$, and $\Gamma = 1$.

to the previous spectrum shown in Fig. 16(b), the broken-$\mathcal{PT}$-symmetric regime produces a comparatively wide and large gain spectrum. For $f = 5$, the system reveals quite a different MI structure compared to the previous case ($f = 0.7$), in which the peculiar MI gain spectrum disappears in the anti-Stokes wave-number regime and the monotonically increasing side gain shifts from the anti-Stokes to the Stokes wave-number region. Further, in the broken-$\mathcal{PT}$-symmetric regime, the primary MI gain spectra emerge on either side of the wave number with pronounced gain and bandwidth, as shown Fig. 16(d).

1. Role of κ in the MI gain spectrum

In this section we analyze the impact of the coupling coefficient κ on the MI gain spectrum in the normal dispersion regime for $f = 0.7$ in the conventional case alone by setting the gain or loss parameter to zero as shown in Fig. 17(a). Interestingly, it shows two different peculiar MI gain spectra that appear around the zero wave number ($K = 0$), where the peculiar MI gain spectrum observed in the anti-Stokes wave-number regime features a wider bandwidth

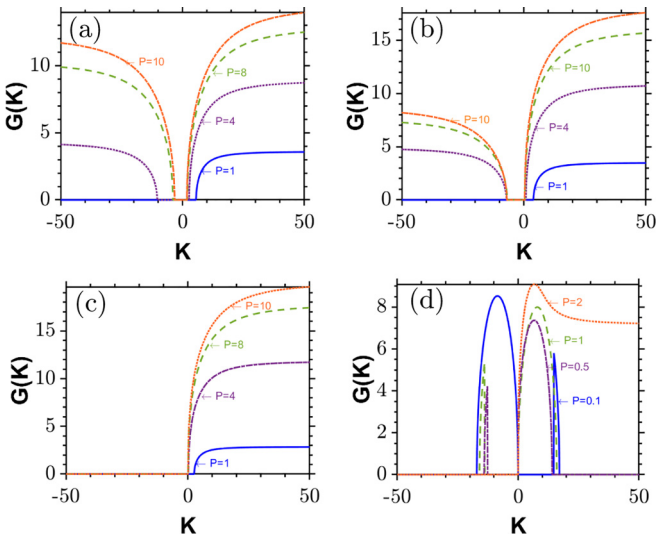

FIG. 18. MI gain spectra as a function of input power in the normal dispersion regime for (a) conventional, (b) below, (c) at, and (d) above $\mathcal{PT}$ thresholds. The parameters are $\kappa = 5$, $\Gamma = 5$, and $f = 0.6$.

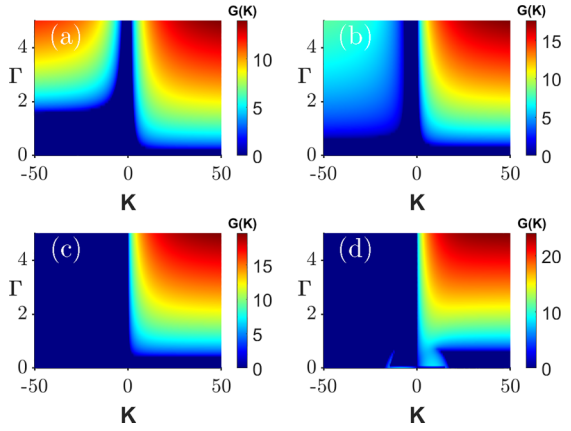

FIG. 19. MI gain spectra with the variations of Γ in the normal dispersion regime for (a) conventional, (b) below, (c) at, and (d) above $\mathcal{PT}$ thresholds. The parameters are $\kappa = 5$, $P = 10$, and $f = 0.6$.

compared to the other one found in the Stokes wave-number region. In particular, the gain of this peculiar MI spectrum is twice as high as in the MI spectrum on the other side, while the bandwidth is about four times wider. It should be stressed that such an unusual MI gain spectrum as a result of the coupling coefficient is a different finding in the context of coupled nonlinear systems. The peak gain traced as a function of κ, displayed in Fig. 17(b), also confirms the same.

2. *Influence of input power P*

We next analyze the effect of power on the characteristics of the instability spectrum in the normal dispersion regime in four different $\mathcal{PT}$-symmetric regimes in Fig. 18. First, in the conventional case [Fig. 18(a)], one can observe a monotonically increasing MI gain only in the anti-Stokes wave-number region for $P = 1$. However, when we increase the value of input power further, the monotonically increasing gain appears on both sides of the wave number. Note that the peak gain in the anti-Stokes wave number is higher than the one in the Stokes wave-number region. The MI characteristics retain the same dynamics and pattern when moving on to the unbroken-$\mathcal{PT}$-symmetric regime, as shown in Fig. 18(b). However, the value of the monotonically increasing gain located in the Stokes wave-number region has been considerably suppressed. When it comes to the case of the $\mathcal{PT}$-symmetric threshold, the monotonically increasing gain in the Stokes wave-number region is completely suppressed while the spectrum found on the other side remains unchanged, which is shown in Fig. 18(c). For the case of the broken-$\mathcal{PT}$-symmetric regime [see Fig. 18(d)], the MI spectrum completely transforms into a typical one for the lower value of the power $P = 0.1$. With a further increase in the value of P, for example, $P = 0.5$ and 1, the spectra get swapped in the different wave-number regions. When we increase the value of P to a higher value such as $P = 2$, the MI sideband located in the anti-Stokes wave-number regime transforms into a monotonically increasing gain, while the MI spectrum on the other side vanishes.

3. *Impact of the nonlinear saturation parameter* Γ

We finally investigate the effect of the nonlinear saturation parameter on the MI gain spectrum in the normal dispersion under four different conditions, including the conventional case as shown in Fig. 19. When $g = 0$ (conventional case) [see Fig. 19(a)], it produces an asymmetric MI structure consisting of two different monotonically increasing gains, where the peak gain in the anti-Stokes wave-number region is more pronounced than the other side. Figure 19(b) depicts the MI dynamics in the unbroken-$\mathcal{PT}$-symmetric regime, where one can observe that the system almost retains the same MI patterns though the range of monotonically increasing gain gets increased in the Stokes wave-number region. Further, when the system is operated at the $\mathcal{PT}$-symmetric threshold, the monotonically increasing gain disappears in the Stokes wave-number region as shown in Fig. 19(c). In contrast to the above, the broken-$\mathcal{PT}$-symmetric regime reveals a narrow sideband in both the Stokes wave-number regions for small values of Γ, as can be seen in Fig. 19(d). Comparing the gain of all these spectra, note that the broken-$\mathcal{PT}$-symmetric produces a relatively higher gain. As the system exhibits rich and complex MI patterns, for an easier and better understanding of the ramifications obtained for various cases, we have provided the summary of the main results in Table I when the system changes from the conventional to different $\mathcal{PT}$-symmetric regimes as a function of g.

V. CONCLUSION

We have investigated theoretically the formation of MI gain spectra in a physical setting of fiber Bragg gratings with saturable nonlinearity and gain and loss. We have found that the obtained nonlinear dispersion curves do not exhibit the loop structure in either the upper branch or the lower branch as opposed to the conventional systems due to the ratio assigned between the different nonlinearities. We have systematically classified our investigation of the MI gain spectrum based on the analysis of the dispersion curves into four cases, namely, the bottom and top of the photonic band gaps and the anomalous and normal dispersions. Having analyzed the dispersion relation first, we then examined the MI gain at the bottom of the photonic band gap. The system has remarkably revealed the emergence of instability spectra with variations in the gain or loss parameter g rather than the function of wave number, in the unbroken-$\mathcal{PT}$-symmetric regime. It is worth mentioning that the finding of such a peculiar MI spectrum is different in the framework of any periodic structures. In addition, the cw manifests in a stable state at the exceptional point and asymmetric spectra tend to appear in the broken-$\mathcal{PT}$-symmetric regime. On the other hand, the role of input power and saturable nonlinearity gives rise to the different MI spectra, namely, the monotonically increasing gain, which further increases with the increase in these parameters. It is interesting to note that in this unbroken-$\mathcal{PT}$-symmetric regime the coupling coefficient has also exhibited the ramification of the peculiar MI bands. The peculiar spectrum persists in the top of the photonic band gap too, accompanied by the conventional symmetric and asymmetric spectra on varying the value of gain or loss parameter. Though the

TABLE I. Summary of the MI gain spectrum obtained in the $\mathcal{PT}$ FBG with saturable nonlinearity. Here Convl denotes Conventional; type-I MI, primary (or symmetric) MI gain spectrum; type-II MI, asymmetric MI sidebands; type-III MI, secondary MI spectrum; type-IV MI, peculiar MI gain spectrum; and type-V, monotonically increasing gain.

	Does the MI gain spectrum exist?				Types of MI gain spectrum			
Types of regimes	Convl case	Unbroken regime	Exceptional point	Broken regime	Convl case	Unbroken regime	Exceptional point	Broken regime
top photonic band gap	no	yes	no	yes	nil	(i) type-IV MI (ii) type-V MI	nil	(i) type-II MI (ii) type-III MI
bottom photonic band gap	yes	yes	yes	yes	type-I MI	type-I MI	type-II MI	(i) type-II MI (ii) type-III MI (iii) type-IV MI
anomalous dispersion	yes	yes	yes	yes	(i) type-II MI (ii) type-III MI	(i) type-II MI (ii) type-III MI	(i) type-V MI (ii) type-IV MI	(i) type-II MI (ii) type-III MI (iii) type-V MI
normal dispersion dispersion	yes	Yes	yes	yes	type-V MI	(i) type-V MI (ii) type-IV MI	type-V MI	(i) type-II MI (ii) type-III MI (iii) type-V MI

coupling coefficient makes the system experience the symmetric spectrum on either side of the zero wave number, the input power and saturable nonlinearity mainly separate the symmetric ones into the multiple structures featuring a primary and a secondary spectrum with a clear manifestation of discreteness in the sidebands. Note that in all the cases, peak gain increases as all the system parameters increase.

The system has shown diverse MI gain spectra for each $\mathcal{PT}$-symmetric regime when it comes to the anomalous dispersion regime. Although the gain or loss parameter has manifested in the complex spectrum when switching from the unbroken- to the broken-$\mathcal{PT}$-symmetric regimes, the increase in both the gain or loss and coupling parameters substantially increases the peak gain of the sidebands in every regime, while the increase in the power and saturable nonlinearity suppresses the spectrum in the anti-Stokes wave-number region. Conversely, in the normal dispersion regime, we have primarily observed the emergence of monotonically increasing gain in addition to the peculiar spectrum when we tune the value of both the coupling coefficient and the gain or loss parameter. In a similar way, the saturable nonlinearity and the input power cause the system to exhibit the monotonically growing gain, which in turn translates into a conventional symmetric MI band when it operates in the above $\mathcal{PT}$ threshold. It is important to stress that all of the instability spectra obtained in this study in various dispersion regimes and under $\mathcal{PT}$-symmetric conditions have qualitative differences from the ones obtained in a conventional Bragg grating structure. We hope that our findings present an opportunity for future studies of localized modes such as Bragg solitons, using the synthetic grating structures that imprint the gain or loss profile.

ACKNOWLEDGMENTS

K.T. acknowledges support from the Department of Science and Technology (DST) and Science and Engineering Research Board (SERB), Government of India, through a National Postdoctoral Fellowship (Grant No. PDF/2021/000167). A.G. was supported by University Grants Commission, Government of India, through a Dr. D. S. Kothari Postdoctoral Fellowship [Grant No. F.4-2/2006(BSR)/PH/19-20/0025]. M.L. was supported by the DST and SERB through a National Science Chair (Grant No. NSC/2020/000029).

[1] C. M. Bender and S. Boettcher, Real Spectra in non-Hermitian Hamiltonians Having $\mathcal{PT}$ Symmetry, Phys. Rev. Lett. **80**, 5243 (1998).

[2] C. M. Bender, D. C. Brody and H. F. Jones, Complex Extension of Quantum Mechanics, Phys. Rev. Lett. **89**, 270401 (2002).

[3] C. M. Bender, D. C. Brody, H. F. Jones, and B. K. Meister, Faster than Hermitian Quantum Mechanics, Phys. Rev. Lett. **98**, 040403 (2007).

[4] R. El-Ganainy, K. Makris, D. Christodoulides, and Z. Musslimani, Theory of coupled optical $\mathcal{PT}$-symmetric structures, Opt. Lett. **32**, 2632 (2007).

[5] K. G. Makris, R. El-Ganainy, D. N. Christodoulides, and Z. H. Musslimani, Beam Dynamics in $\mathcal{PT}$-Symmetric Optical Lattices, Phys. Rev. Lett. **100**, 103904 (2008).

[6] K. G. Makris, R. El-Ganainy, and D. N. Christodoulides, $\mathcal{PT}$-symmetric optical lattices, Phys. Rev. A **81**, 063807 (2010).

[7] C. E. Rüter, K. G. Makris, R. El-Ganainy, D. N. Christodoulides, M. Segev, and D. Kip, Observation of parity-time symmetry in optics, Nat. Phys. **6**, 192 (2010).

[8] A. Guo, G. J. Salamo, D. Duchesne, R. Morandotti, M. Volatier-Ravat, V. Aimez, G. A. Siviloglou, and D. N. Christodoulides, Observation of $\mathcal{PT}$-Symmetry Breaking in Complex Optical Potentials, Phys. Rev. Lett. **103**, 093902 (2009).

[9] A. Govindarajan, A. K. Sarma, and M. Lakshmanan, Tailoring $\mathcal{PT}$-symmetric soliton switch, Opt. Lett. **44**, 663 (2019).

[10] A. Regensburger, C. Bersch, M. A. Miri, G. Onischchukov, D. N. Christodoulides, and U. Peschel, Parity-time synthetic photonic lattices, Nature (London) **488**, 167 (2012).

[11] S. Weimann, M. Kremer, Y. Plotnik, Y. Lumer, S. Nolte, K. G. Makris, M. Segev, M. C. Rechtsman, and A. Szameit, Topologically protected bound states in photonic parity-time-symmetric crystals, Nat. Mater. **16**, 433 (2017).

[12] J. Li, A. K. Harter, J. Liu, L. de Melo, Y. N. Joglekar, and L. Luo, Observation of parity-time symmetry breaking transitions in a dissipative Floquet system of ultracold atoms, Nat. Commun. **10**, 855 (2019).

[13] S. Phang, A. Vukovic, T. M. Benson, H. Susanto, and P. Sewell, A versatile all-optical parity-time signal processing device using a Bragg grating induced using positive and negative Kerr-nonlinearity, Opt. Quantum Electron. **47**, 37 (2015).

[14] T. Kottos, Broken symmetry makes light work, Nat. Phys. **6**, 166 (2010).

[15] S. V. Suchkov, A. A. Sukhorukov, J. Huang, S. V. Dmitriev, C. Lee, and Y. S. Kivshar, Nonlinear switching and solitons in $\mathcal{PT}$-symmetric photonic systems, Laser Photon. Rev. **10**, 177 (2016).

[16] V. V. Konotop, J. Yang, and D. A. Zezyulin, Nonlinear waves in $\mathcal{PT}$-symmetric systems, Rev. Mod. Phys. **88**, 035002 (2016).

[17] C. R. Giles, Lightwave applications of fiber Bragg gratings, J. Lightw. Technol. **15**, 1391 (1997).

[18] R. Kashyap, *Fiber Bragg Gratings* (Academic, New York, 2010).

[19] K. O. Hill and G. Meltz, Fiber Bragg grating technology fundamentals and overview, J. Lightw. Technol. **15**, 1263 (1997).

[20] P. S. J. Russell, Bloch wave analysis of dispersion and pulse propagation in pure distributed feedback structures, J. Mod. Opt. **38**, 1599 (1991).

[21] H. A. Hans, *Waves and Fields in Optoelectronics* (Prentice-Hall, Englewood Cliffs, 1984); D. Marcuse, *Theory of Dielectric Optical Waveguides* (Academic, San Diego, 1991).

[22] A. Yariv, *Optical Electronics in Modern Communications*, 5th ed. (Oxford University Press, New York, 1997).

[23] Y. Kivshar and G. Agrawal, *Optical Solitons: From Fibers to Photonic Crystals* (Academic, New York, 2001).

[24] N. M. Litchinitser, B. J. Eggleton, C. M. de Sterke, A. B. Aceves, and G. P. Agrawal, J. Opt. Soc. Am. B **16**, 18 (1999); W. C. K. Mak, B. A. Malomed, and P. L. Chu, Interaction of a soliton with a local defect in a fiber Bragg grating, *ibid.* **20**, 725 (2003).

[25] D. Taverner, N. Broderick, D. Richardson, M. Ibsen, and R. Laming, All-optical and gate based on coupled gap-soliton formation in a fiber Bragg grating, Opt. Lett. **23**, 259 (1998).

[26] S. Vignesh Raja, A. Govindarajan, A. Mahalingam, and M. Lakshmanan, Multifaceted dynamics and gap solitons in $\mathcal{PT}$-symmetric periodic structures, Phys. Rev. A **100**, 033838 (2019).

[27] I. V. Kabakova, T. Walsh, C. M. de Sterke, and B. J. Eggleton, Performance of field-enhanced optical switching in fiber Bragg gratings, J. Opt. Soc. Am. B **27**, 1343 (2010); S. Vignesh Raja, A. Govindarajan, A. Mahalingam, and M. Lakshmanan, Tailoring inhomogeneous $\mathcal{PT}$-symmetric fiber Bragg grating spectra, Phys. Rev. A **101**, 033814 (2020).

[28] Q. Li, K. Senthilnathan, K. Nakkeeran, and P. K. A. Wai, Nearly chirp- and pedestal-free pulse compression in nonlinear fiber Bragg gratings, J. Opt. Soc. Am. A **26**, 432 (2009); Q. Li, P. K. A. Wai, K. Senthilnathan, and K. Nakkeeran, Modeling self-similar optical pulse compression in nonlinear fiber Bragg grating using coupled-mode equations, J. Lightw. Technol. **29**, 1293 (2011).

[29] H. G. Winful, J. Marburger, and E. Garmire, Theory of bistability in nonlinear distributed feedback structures, Appl. Phys. Lett. **35**, 379 (1979); C.-X. Shi, Optical bistability in reflective fiber gratings, IEEE J. Quantum Electron. **31**, 2037 (1995).

[30] C. M. de Sterke, Theory of modulational instability in fiber Bragg gratings, J. Opt. Soc. Am. B **15**, 2660 (1998); K. Porsezian, K. Senthilnathan, and S. Devipriya, Modulational instability in fiber Bragg grating with non-Kerr nonlinearity, IEEE J. Quantum Electron. **41**, 789 (2005); B. Kalithasan, K. Porsezian, K. Senthilnathan, and P. Tchofo Dinda, Generation of self-induced-transparency gap solitons by modulational instability in uniformly doped fiber Bragg gratings, Phys. Rev. A **81**, 053802 (2010).

[31] M. A. Miri, A. B. Aceves, T. Kottos, V. Kovanis, and D. N. Christodoulides, Optical mesh lattices with $\mathcal{PT}$ symmetry, Phys. Rev. A **86**, 023807 (2012).

[32] F. Correa and V. Jakubský, Confluent Crum-Darboux transformations in Dirac Hamiltonians with $\mathcal{PT}$-symmetric Bragg gratings, Phys. Rev. A **95**, 033807 (2017).

[33] Z. Lin, H. Ramezani, T. Eichelkraut, T. Kottos, H. Cao, and D. N. Christodoulides, Unidirectional Invisibility Induced by $\mathcal{PT}$-Symmetric Periodic Structures, Phys. Rev. Lett. **106**, 213901 (2011)

[34] Y. Sun, W. Tan, H. Li, J. Li, and H. Che, Experimental Demonstration of a Coherent Perfect Absorber with PT Phase Transition, Phys. Rev. Lett. **112**, 143903 (2014).

[35] L. Poladian, Resonance mode expansions and exact solutions for nonuniform gratings, Phys. Rev. E **54**, 2963 (1996).

[36] M. Kulishov, J. M. Laniel, N. Bélanger, J. Azaña, and D. V. Plant, Nonreciprocal waveguide Bragg gratings, Opt. Express **13**, 3068 (2005).

[37] K. Tai, A. Hasegawa, and A. Tomita, Observation of Modulational Instability in Optical Fibers, Phys. Rev. Lett. **56**, 135 (1986).

[38] Y. Kominis, T. Bountis, and S. Flach, Stability through asymmetry: Modulationally stable nonlinear supermodes of asymmetric non-Hermitian optical couplers, Phys. Rev. A **95**, 063832 (2017).

[39] A. Hasegawa, Generation of a train of soliton pulses by induced modulational instability in optical fibers, Opt. Lett. **9**, 288 (1984).

[40] T. B. Benjamin and J. E. Feir, The disintegration of wave trains on deep water, J. Fluid Mech. **27**, 417 (1967).

[41] M. Remoissent, *Waves Called Solitons* (Springer, Berlin, 1999).

[42] N. Akhtar, S. Mahmood, N. Jehan, and A. M. Mirza, Modulational instability of electrostatic waves in a magnetized dusty plasma with kappa distributed electrons, Phys. Plasmas **24**, 113707 (2017).

[43] G. Van Simaeys, P. Emplit, and M. Haelterman, Experimental Demonstration of the Fermi-Pasta-Ulam Recurrence in a Modulationally Unstable Optical Wave, Phys. Rev. Lett. **87**, 033902 (2001).

[44] M. Erkintalo, K. Hammani, B. Kibler, C. Finot, N. Akhmediev, J. M. Dudley, and G. Genty, Higher-Order Modulation

Instability in Nonlinear Fiber Optics, Phys. Rev. Lett. **107**, 253901 (2011).

[45] A. E. Kraych, P. Suret, G. El, and S. Randoux, Nonlinear Evolution of the Locally Induced Modulational Instability in Fiber Optics, Phys. Rev. Lett. **122**, 054101 (2019).

[46] V. E. Zakharov and A. A. Gelash, Nonlinear Stage of Modulation Instability, Phys. Rev. Lett. **111**, 054101 (2013).

[47] E. J. Greer, D. M. Patrick, P. G. J. Wigley, and J. R. Taylor, Generation of 2 THz repetition rate pulse trains through induced modulational instability, Electron. Lett. **25**, 1246 (1989).

[48] J. M. Dudley, G. Genty, F. Dias, B. Kibler, and N. Akhmediev, Modulation instability, Akhmediev breathers and continuous wave supercontinuum generation, Opt. Express **17**, 21497 (2009).

[49] F. Leo, T. Hansson, I. Ricciardi, M. De Rosa, S. Coen, S. Wabnitz, and M. Erkintalo, Walk-Off-Induced Modulation Instability, Temporal Pattern Formation, and Frequency Comb Generation in Cavity-Enhanced Second-Harmonic Generation, Phys. Rev. Lett. **116**, 033901 (2016).

[50] P. Del'Haye, A. Schliesser, O. Arcizet, T. Wilken, R. Holzwarth, and T. J. Kippenberg, Optical frequency comb generation from a monolithic microresonator, Nature (London) **450**, 1214 (2007).

[51] V. E. Zakharov and L. A. Ostrovsky, Modulation instability: The beginning, Physica D **238**, 540 (2009).

[52] N. M. Litchinitser, C. J. McKinstrie, C. M. de Sterke, and G. P. Agrawal, Spatiotemporal instabilities in nonlinear bulk media with Bragg gratings, J. Opt. Soc. Am. B **18**, 45 (2001).

[53] A. Joseph, K. Senthilnathan, K. Porsezian, and P. T. Dinda, Gap solitons and modulation instability in a dynamic Bragg grating with nonlinearity management, J. Opt. A **11**, 015203 (2009).

[54] J.-L. Coutaz and M. Kull, Saturation of the nonlinear index of refraction in semiconductor-doped glass, J. Opt. Soc. Am. B **8**, 95 (1991).

[55] J. M. Hickmann, S. B. Cavalcanti, N. M. Borges, E. A. Gouveia, and A. S. Gouveia-Neto, Modulational instability in semiconductor-doped glass fibers with saturable nonlinearity, Opt. Lett. **18**, 182 (1993).

[56] J. M. Soto-Crespo, D. R. Heatley, E. Wright, and N. N. Akhmediev, Stability of the higher-bound states in a saturable self-focusing medium, Phys. Rev. A **44**, 636 (1991).

[57] N. Akhmediev and J. M. Soto-Crespo, Generation of a train of three-dimensional optical solitons in a self-focusing medium, Phys. Rev. A **47**, 1358 (1993); T. K. Gustafson, P. L. Kelley, R. Y. Chiao, and R. G. Brewer, Self-trapping in media with saturation of the nonlinear index, Appl. Phys. Lett. **12**, 165 (1968); J. H. Marburger and E. Dawes, Dynamical Formation of a Small-Scale Filament, Phys. Rev. Lett. **21**, 556 (1968).

[58] F. Chen, M. Stepić, C. E. Rüter, D. Runde, D. Kip, V. Shandarov, O. Manela, and M. Segev, Discrete diffraction and spatial gap solitons in photovoltaic $LiNbO_3$ waveguide arrays, Opt. Express **13**, 4314 (2005).

[59] G. L. da Silva, I. Gleria, M. L. Lyra, and A. S. B. Sombra, Modulational instability in lossless fibers with saturable delayed nonlinear response, J. Opt. Soc. Am. B **26**, 183 (2009).

[60] P. T. Dinda and K. Porsezian, Impact of fourth-order dispersion in the modulational instability spectra of wave propagation in glass fibers with saturable nonlinearity, J. Opt. Soc. Am. B **27**, 1143 (2010).

[61] I. M. Merhasin, B. A. Malomed, K. Senthilnathan, K. Nakkeeran, P. K. A. Wai, and K. W. Chow, Solitons in Bragg gratings with saturable nonlinearity, J. Opt. Soc. Am. B **24**, 1458 (2007).

[62] A. K. Sarma, Modulation instability in nonlinear complex parity-time symmetric periodic structures, J. Opt. Soc. Am. B **31**, 1861 (2014).

[63] S. Vignesh Raja, A. Govindarajan, A. Mahalingam, and M. Lakshmanan, Nonlinear nonuniform $\mathcal{PT}$-symmetric Bragg grating structures, Phys. Rev. A **100**, 053806 (2019).

[64] J. Liu, X. T. Xie, C. J. Shan, T. K. Liu, R. K. Lee, and Y. Wu, Optical bistability in nonlinear periodical structures with $\mathcal{PT}$-symmetric potential, Laser Phys. **25**, 015102 (2015).

[65] X. Zhong and A. Xiang, Cross-phase modulation induced modulation instability in single-mode optical fibers with saturable nonlinearity, Opt. Fiber Technol. **13**, 271 (2007).

[66] M. L. Lyra and A. S. Gouveia-Neto, Saturation effects on modulation instability in non-Kerr-like monomode optical fibers, Opt. Commun. **108**, 117 (1994); X. Q. Zhong and A. P. Xiang, Cross-phase modulation instability in single-mode optical fibers with exponential saturable nonlinearity, Chin. Phys. B **19**, 110310 (2010); C. G. Latchio, A. Mohamadou, Alim, K. Porsezian, and T. C. Kofane, Modulational instability in metamaterials with saturable nonlinearity and higher-order dispersion, J. Mod. Opt. **59**, 972 (2012); W. Krolikowski and B. Luther-Davies, Dark optical solitons in saturable nonlinear media, Opt. Lett. **18**, 188 (1993).

[67] R. W. Boyd, *Nonlinear Optics*, 3rd ed. (Academic, New York, 2008).

[68] C. Pan, L. Bu, S. Chen, D. Mihalache, P. Grelu, and F. Baronio, Omnipresent coexistence of rogue waves in a nonlinear two-wave interference system and its explanation by modulation instability, Phys. Rev. Res. **3**, 033152 (2021).